

Excitonic effects at the temperature-dependent direct bandgap of Ge

Cite as: J. Appl. Phys. **131**, 165701 (2022); <https://doi.org/10.1063/5.0080158>

Submitted: 29 November 2021 • Accepted: 28 March 2022 • Published Online: 25 April 2022

 Carola Emminger,  Nuwanjula S. Samarasingha, Melissa Rivero Arias, et al.



View Online



Export Citation



CrossMark

ARTICLES YOU MAY BE INTERESTED IN

[On the kinetics of the exchange of hydrogen between hydrogen-boron pairs and hydrogen dimers in crystalline silicon](#)

Journal of Applied Physics **131**, 165702 (2022); <https://doi.org/10.1063/5.0086307>

[Hexagonal close-packed \(hcp\) alloys under dynamic impacts](#)

Journal of Applied Physics **131**, 165902 (2022); <https://doi.org/10.1063/5.0085338>

[Acoustic phonons and elastic stiffnesses from Brillouin scattering of CdPS₃](#)

Journal of Applied Physics **131**, 165109 (2022); <https://doi.org/10.1063/5.0084258>

Lock-in Amplifiers
up to 600 MHz



Zurich
Instruments



Excitonic effects at the temperature-dependent direct bandgap of Ge

Cite as: J. Appl. Phys. **131**, 165701 (2022); doi: [10.1063/5.0080158](https://doi.org/10.1063/5.0080158)

Submitted: 29 November 2021 · Accepted: 28 March 2022 ·

Published Online: 25 April 2022



Carola Emminger,^{1,2,a)} Nuwanjula S. Samarasingha,¹ Melissa Rivero Arias,¹ Farzin Abadizaman,² José Menéndez,³ and Stefan Zollner¹

AFFILIATIONS

¹Department of Physics, New Mexico State University, Las Cruces, New Mexico 88003-8001, USA

²Department of Condensed Matter Physics, Masaryk University, 61137 Brno, Czech Republic

³Department of Physics, Arizona State University, Tempe, Arizona 85287-1504, USA

^{a)}Author to whom correspondence should be addressed: emminge@nmsu.edu.

ABSTRACT

The temperature dependence of the complex dielectric function $\epsilon_1 + i\epsilon_2$ of bulk Ge near the direct bandgap was investigated with spectroscopic ellipsometry at temperatures between 10 and 710 K. Second derivatives of the dielectric function with respect to energy are obtained using a digital linear filter method. A model that incorporates excitonic effects using the Tanguy model for the Hulthén potential [C. Tanguy, Phys. Rev. B **60**, 10660 (1999)] was used to fit the dielectric function and its second derivatives simultaneously. Using $k \cdot p$ theory and literature values for effective masses, reasonable agreement with the experiment is obtained for ϵ_2 up to room temperature using the direct bandgap and its broadening as the only adjustable parameters.

Published under an exclusive license by AIP Publishing. <https://doi.org/10.1063/5.0080158>

I. INTRODUCTION

Photo-excited electron-hole pairs in semiconductors form excitonic bound states, because the negatively charged electron and the positively charged hole are attracted to each other by the Coulomb force, similar to a hydrogen atom. The Bohr model gives a reasonable description of excitonic effects in semiconductors, as long as the effective masses of electrons and holes replace the masses of the proton and free electron, respectively, and the electrostatic screening is taken into account using the static dielectric constant. This electron-hole interaction not only results in discrete excitonic peaks below the bandgap, but also it leads to the so-called Sommerfeld enhancement of the absorption above the bandgap.¹

While the physics of excitonic effects has been understood for decades,²⁻⁴ a quantitative comparison of these theories with experimental data for the dielectric function of semiconductors near the direct bandgap E_0 has, to the best of our knowledge, never been attempted. The goal of this work is to fit the dielectric function (and its second derivative) of Ge near E_0 from 10 to 710 K with only two adjustable parameters that describe the influence of E_0 : the bandgap energy and the broadening at each temperature. Our model will have important applications for optoelectronic devices such as detectors

and lasers. It can be applied not only to Ge, but also to other materials, such as GaAs, InSb, or germanium-tin alloys.

In a recent publication,⁵ we presented results on the temperature dependence of the direct bandgap energy and broadening of bulk Ge, obtained from spectroscopic ellipsometry (SE). The E_0 energy was determined by a Fourier or reciprocal space⁶ (RS) analysis, without assuming a specific line shape, as well as by fitting a three-dimensional (3D) standard analytical line shape^{7,8} to the numerically calculated⁹ second derivatives (SD) with respect to energy, and by applying a parametric semiconductor model.¹⁰ However, the assumption of a 3D line shape does not deliver a satisfactory description of the absorption edge of Ge due to the presence of excitonic effects.^{11,12} An analytical expression for optical absorption by excitons was published by Elliott² and the theory was expanded to the complex dielectric function by Tanguy.³ The bare excitonic Coulomb interaction in semiconductor materials can be screened by mobile carriers, and this leads to a Yukawa-like potential for which there are no analytical solutions to the excitonic problem. However, it has been shown that a remarkably accurate substitution for the Yukawa interaction is the Hulthén potential,¹³ for which Tanguy⁴ has found analytical expressions for the

complex dielectric function. In the limit of negligible screening, applicable to intrinsic Ge at room temperature and below, the dielectric function for the Hulthén potential becomes identical to the dielectric function found by Tanguy for the bare Coulomb potential. At the highest temperatures in our experiments, however, the intrinsic carrier concentration increases by several orders of magnitude to values comparable to the critical Mott concentration¹⁴ and, therefore, screening effects may be substantial. Accordingly, we use the Tanguy solution for the Hulthén potential to fit the dielectric function and its second derivative. The latter is obtained using a digital linear filter method^{15–17} based on extended Gauss functions.^{18,19}

The Hulthén–Tanguy model depends on the bandgap energy, a Lorentzian broadening parameter, the exciton binding energy, an amplitude, a momentum matrix element, and a screening parameter. The amplitude, momentum matrix element, and excitonic binding energy can be obtained from $k \cdot p$ theory and fit to the band structure. The screening parameter is computed from a standard expression for the Thomas–Fermi screening wave vectors, following a prescription from Ref. 20. This leaves only two adjustable parameters for the Hulthén model: energy and broadening of the direct gap. We add a Sellmeier term with two additional adjustable parameters to consider contributions from critical points at higher energies to the real part of the dielectric function. We simply combine the heavy-hole (hh) and light-hole (lh) excitonic dielectric functions as if they were additive. This is not strictly correct but it has been shown to be a good approximation.^{20,21}

Recent work²⁰ on phonon-assisted indirect absorption in Ge shows that this absorption is strongly resonant at the direct bandgap. A satisfactory theory including phonon-assisted processes for photon energies above the direct gap is not available at this time, and one cannot rule out a significant contribution in a range that was traditionally believed to be accounted mainly by direct transitions. Unfortunately, previous fits of the dielectric function in this range relied on adjustable amplitude parameters that are not well described by theory and on the introduction of phase factors that account for excitonic effects very indirectly. Due to the *ad hoc* character of the parameters, the issue of whether the above gap absorption is truly dominated by direct transitions could not be addressed. The new model that we present in this paper treats excitonic effects explicitly and relies on known material parameters to calculate those “amplitudes.” By accounting for direct absorption in a realistic way, it creates a basic framework from which the impact of additional contributions to the absorption, such as phonon-assisted processes, can be evaluated and quantified.

II. EXPERIMENT

The dielectric function in the region of the direct bandgap of a commercially obtained undoped bulk Ge sample with (100) surface orientation was measured between 80 and 710 K using a J.A. Woollam VASE ellipsometer²² with a xenon light source (190 nm–2 μ m) and a Janis ST-400 UHV cryostat. The Ge wafer was undoped with a resistivity higher than 50 Ω cm, which indicates an electron or hole concentration no higher than 10¹⁴ cm^{−3} at room temperature.²³

We used liquid nitrogen to cool the system for the measurements between 80 K and room temperature. The sample was

TABLE I. Experimental parameters: Slit width (s), step size ($\Delta E'$), and native oxide layer thickness (d). An iris was installed at the exit window of the cryostat for measurements above 400 K. ΔE is the width of the linear filter used to calculate the second energy derivatives (see Sec. IV).

Temperature (K)	s (μ m)	$\Delta E'$ (meV)	d (Å)	Iris	ΔE (meV)
10 ^a	500	0.5	11	No	1.0
80–300	400	0.4	12–13	No	0.9–1.6
323–368	400	0.4	9–11	No	1.8–4.0
391	400	0.4	9	Yes	4.0–4.5
412–436	500	0.4	9	Yes	3.5
458–479	900	0.4	8	Yes	3.5–4.0
500–542	1000	0.4	8	Yes	4.0–4.5
559	800	0.4	8	Yes	5.0
578–676	1500	0.4	8	Yes	5.0–7.0
690–710	1700	0.4	7–8	Yes	8.0

^aReference 5.

cleaned in an ultrasonic bath in isopropanol for 20 min, followed by an ultrasonic bath in ultrapure water for another 20 min, which reduced the native oxide layer thickness from 4 to about 1 nm. After cleaning, the sample was immediately mounted into the UHV cryostat and heated up to 635 K for about 8 h for degassing and to stabilize the native oxide layer. At temperatures $T \geq 391$ K, we installed an iris at the exit window of the cryostat to suppress effects due to blackbody radiation, as illustrated in Fig. S4 in Ref. 5. To better resolve the narrow structure of the excitonic peak, we used a slightly smaller step size (0.4 meV) than in our previous work.⁵ A slit width between 400 and 1700 μ m was chosen for our J.A. Woollam Co. HS-190 monochromator in order to achieve an instrumental resolution of about 1–2.5 meV and a satisfactory signal-to-noise ratio at each temperature. Experimental parameters at the various temperatures are listed in Table I. We also analyze the data set from Ref. 5 measured at 10 K with a step size of 0.5 meV and slit width of 500 μ m.

A two-layer model (substrate+native oxide layer) was used to perform an oxide correction of the pseudodielectric function and to extract the dielectric function, as explained elsewhere.^{24,25} The thickness of the native oxide layer varied between 12 and 13 Å at and below room temperature and 7–11 Å at higher temperatures. A similar approach was used by others to measure the optical functions of silicon at high temperatures up to 1200 K.²⁶

III. HULTHÉN-TANGUY MODEL

To describe excitonic effects at the direct bandgap of Ge, we use the expression for the complex dielectric function given by the Tanguy model for the Hulthén potential,⁴

$$\epsilon(E) = \frac{A\sqrt{R}}{(E + i\gamma)^2} [\tilde{g}(\xi(E + i\gamma)) + \tilde{g}(\xi(-E - i\gamma)) - 2\tilde{g}(\xi(0))], \quad (1)$$

with

$$\xi(z) = \frac{2}{\left(\frac{E_0 - z}{R}\right)^{1/2} + \left(\frac{E_0 - z}{R} + \frac{4}{g}\right)^{1/2}} \quad (2)$$

and

$$\tilde{g}(\xi) = -2\psi\left(\frac{g}{\xi}\right) - \frac{\xi}{g} - 2\psi(1 - \xi) - \frac{1}{\xi}, \quad (3)$$

where $\psi(z)$ is the digamma function, A is the amplitude, R is the excitonic binding energy, γ is the broadening, and E_0 is the direct bandgap energy. The Hulthén screening parameter g depends on the carrier concentration and is set to $g = 35$ for undoped Ge, according to Fig. 5 in Ref. 21. However, g is not independent of temperature due to the temperature-dependent carrier concentration (see Fig. S3 in the supplementary material). The four terms in Eq. (3) define the line shape of the direct bandgap, which is illustrated in Fig. 1. We define $\epsilon(E) = \epsilon_1(E) + i\epsilon_2(E) = \sum_{j=1}^4 f_j$ with

$$f_1 = -2\beta \left[\psi\left(\frac{g}{\xi(z_1)}\right) + \psi\left(\frac{g}{\xi(z_2)}\right) + \psi\left(\frac{g}{\xi(0)}\right) \right], \quad (4)$$

$$f_2 = -\frac{\beta}{g} [\xi(z_1) + \xi(z_2) + \xi(0)], \quad (5)$$

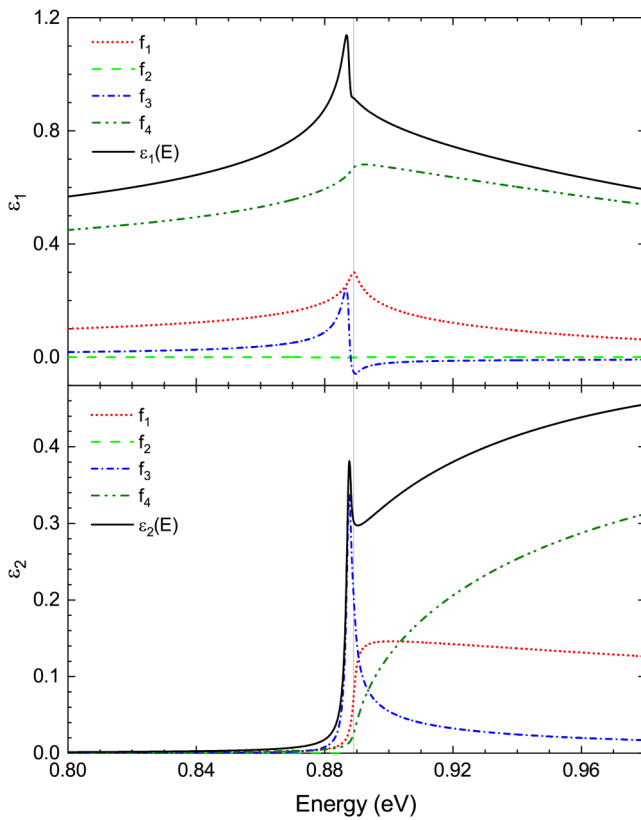


FIG. 1. Real and imaginary parts of the terms in Eq. (1), defined in Eqs. (4)–(7), with $E_0 = 0.889$ eV (marked by the vertical line), $\gamma = 1$ meV, $R = 1.5$ meV, $A = 1.0$ eV $^{-3/2}$, and $g = 35$. The solid line represents the dielectric function as defined in Eq. (1), which is equivalent to the sum of the four terms f_1 – f_4 in Eqs. (4)–(7). For $g \rightarrow \infty$, $f_2 \rightarrow 0$.

$$f_3 = -2\beta[\psi(1 - \xi(z_1)) + \psi(1 - \xi(z_2)) + \psi(1 - \xi(0))], \quad (6)$$

and

$$f_4 = -\frac{\beta}{\xi(z_1)} - \frac{\beta}{\xi(z_2)} - \frac{\beta}{\xi(0)}, \quad (7)$$

where $\beta = A\sqrt{R}(E + i\gamma)^{-2}$, $z_1 = E + i\gamma$, and $z_2 = -E - i\gamma$. The first term, f_1 , describes the enhancement due to the exciton continuum (unbound excitons), f_3 describes the peak of the bound exciton, and f_4 is equal to an M_0 three-dimensional critical point line shape,¹ which describes the absorption edge without excitonic effects. For large screening parameters, i.e., $g \gg 1$, the screening term f_2 given by Eq. (5) vanishes.

The Hulthén–Tanguy model assumes spherical parabolic bands,^{2–4} as well as one conduction and one valence band, but since two degenerate valence bands (hh and lh) are present at the Γ -point of Ge, one would have to solve a complicated three-body problem.²¹ However, the error made by adding separate hh- and lh-excitons is small, as discussed in Refs. 20 and 21, and, therefore, we use separate terms for hh and lh. To take into account contributions from the E_1 critical point to the real part of the dielectric function, we add a single term from the Sellmeier dispersion formula, i.e., $1 + A_1/(1 - B_1^2 E^2)$,^{27,28} where we treat the parameters A_1 and $B_1' = B_1/(2\pi c\hbar)$ as adjustables. Values for A_1 and B_1' for Ge can be found in Ref. 28 ($A_1 \approx 14.76$, $B_1' \approx 0.35$ eV $^{-1}$). Since the split-off band contribution $E_0 + \Delta_0$ is small and only affects the real part of the dielectric function, which can be compensated by adapting the Sellmeier parameters, we do not include an additional term for the split-off band. Following these considerations, the expression that we use for the fits is

$$\begin{aligned} \epsilon(E) = & 1 + \frac{A_1}{1 - B_1'^2 E^2} \\ & + \frac{A_{hh}\sqrt{R_{hh}}}{(E + i\gamma_{hh})^2} [\tilde{g}(\xi(E + i\gamma_{hh})) + \tilde{g}(\xi(-E - i\gamma_{hh})) - 2\tilde{g}(\xi(0))] \\ & + \frac{A_{lh}\sqrt{R_{lh}}}{(E + i\gamma_{lh})^2} [\tilde{g}(\xi(E + i\gamma_{lh})) + \tilde{g}(\xi(-E - i\gamma_{lh})) - 2\tilde{g}(\xi(0))], \end{aligned} \quad (8)$$

where γ_{hh} and γ_{lh} are the hh- and lh-broadening parameters, respectively. The excitonic amplitude is given by Ref. 1

$$A_h = \frac{e^2 \sqrt{m_0}}{\sqrt{2\pi\epsilon_0\hbar}} \mu_h^{3/2} \frac{E_P}{3}, \quad (9)$$

where $h = hh, lh$, e is the electron charge, m_0 is the free electron mass, ϵ_0 is the vacuum permittivity, μ_h is the reduced mass calculated from the effective mass of the hh or lh and the effective mass of the electron in the Γ -valley, and $E_P = 2P^2/m_0$, with P being the $k \cdot p$ momentum matrix element corresponding to interband transitions between the Γ'_{25} valence band and the Γ'_2 conduction band. From the reduced mass $\mu_h = m_h m_{e\Gamma}/(m_h + m_{e\Gamma})$ and the Rydberg energy of the hydrogen atom $R_y = 13.6$ eV, the excitonic binding

energy is calculated by

$$R_h = \frac{\mu_h}{m_0 \epsilon_{st}^2} R_y, \quad (10)$$

where ϵ_{st} is the static dielectric constant. The effective mass $m_{e\Gamma}$ of the electron in the Γ -valley is related to E_p and E_0 ,^{29–31}

$$\frac{m_0}{m_{e\Gamma}} = 1 + \frac{E_p}{3} \left[\frac{2}{E_0} + \frac{1}{E_0 + \Delta_0} \right], \quad (11)$$

where $\Delta_0 = 0.29 \text{ eV}$ ^{5,32} is the temperature independent spin-orbit splitting at the Γ -point. The hh and lh effective masses are given by Ref. 33,

$$\frac{m_0}{m_{hh}} = \frac{1}{\hbar^2} \left[-A + \sqrt{B^2 + C^2/5} \right] \quad (12)$$

and

$$\frac{m_0}{m_{lh}} = \frac{1}{\hbar^2} \left[-A - \sqrt{B^2 + C^2/5} \right], \quad (13)$$

where A , B , and C are parameters introduced by Dresselhaus, Kip, and Kittel³⁴ (DKK), which are defined as^{31,34}

$$A = \frac{1}{3} [F + 2G + 2M] + 1, \quad (14)$$

$$B = \frac{1}{3} [F + 2G - M], \quad (15)$$

$$C^2 = \frac{1}{3} [(F - G + M)^2 - (F + 2G - M)^2]. \quad (16)$$

The DKK parameters A , B , and C^2 depend on temperature via¹

$$F(T) = -E_p(T)/E_0(T), \quad (17)$$

$$M(T) = -E_Q(T)/E'_0(T), \quad (18)$$

$$G(T) = G(4.2 \text{ K}) \frac{a_0^2(4.2 \text{ K})}{a_0^2(T)}. \quad (19)$$

The temperature dependence of E'_0 is taken from Ref. 25,

$$E'_0(T) = (3.18 \text{ eV}) - (0.05 \text{ eV}) \left(1 + \frac{2}{e^{\frac{313\text{K}}{T}} - 1} \right). \quad (20)$$

In Eq. (18), $E_Q = 2Q^2/m_0$, and Q is the non-zero matrix element corresponding to interband transitions between the Γ'_{25} valence band and the Γ'_{15} conduction band.^{1,31} Thermal expansion causes a temperature dependence of the matrix elements $M = P, Q$ given by

TABLE II. Parameters at 4.2 K, determined as explained in the text. Effective and reduced masses are given in units of m_0 .

$m_{e\Gamma}$	m_{hh}	m_{lh}	μ_{hh}	μ_{lh}	A_{hh}	A_{lh}	R_{hh} (meV)	R_{lh} (meV)
0.036	0.33	0.042	0.032	0.019	0.74	0.35	1.8	1.1

Ref. 20,

$$E_M(T) = E_M(4.2 \text{ K}) \times \frac{a_0^2(4.2 \text{ K})}{a_0^2(T)}, \quad (21)$$

via the temperature-dependent lattice constant

$$a_0(T) = (5.6516 \text{ \AA}) + \frac{\delta}{\exp(T_0/T) - 1}, \quad (22)$$

where $\delta = 1.315 \times 10^{-2} \text{ \AA}$ and $T_0 = 355.14 \text{ K}$ are parameters describing thermal expansion of the Ge lattice.²⁰ The change of the matrix elements with temperature is small (less than 1% between 0 and 800 K). Therefore, the major contribution to the temperature dependence of the DKK parameters and consequently of the effective masses stems from the energy gaps.

Equation (19) specifies the contribution related to the matrix element R between Γ'_{25} and Γ'_{12} .^{1,31} Since the temperature dependence of this gap is not known, we use $A = -13.34$, $B = -8.48$, and $|C| = 13.14$ at 4.2 K from Ref. 20 in order to find exact low-temperature solutions. Using $E_0(4.2 \text{ K}) = 0.889 \text{ eV}$,³⁵ we obtain $E_p(4.2 \text{ K}) = 26.0 \text{ eV}$ (which is close to the value of 26.3 eV reported by Lawaetz³⁶), $E_Q(4.2 \text{ K}) = 18.5 \text{ eV}$, and $G(4.2 \text{ K}) = -1.04$. Table II lists the resulting effective and reduced masses, amplitudes, and excitonic binding energies at liquid He temperature. The conduction band effective mass $m_{e\Gamma}$ agrees well with $m_{e\Gamma} = 0.037 m_0$ reported by Roth *et al.*³⁷ and $m_{e\Gamma} = 0.038 m_0$ by Lawaetz,³⁶ and the calculated hh and lh masses are in reasonable agreement with the values found by Lawaetz³⁶ ($m_{hh} = 0.35 m_0$ and $m_{lh} = 0.043 m_0$).

IV. SECOND DERIVATIVES THROUGH LINEAR FILTERING

To obtain the second energy derivatives, we apply the linear filter method using Gaussian kernels by Le *et al.*,¹⁶ which is based on a direct space convolution,

$$\bar{f}(E) = \int_{-\infty}^{\infty} dE' f(E') b_M(E - E'), \quad (23)$$

with extended Gauss (EG)^{16,18,19} filters

$$b_M(x) = \sum_{m=0}^M \left((-1)^m \frac{a^m}{m!} \frac{d^m}{da^m} \right) \frac{a^{-\frac{1}{2}}}{2\sqrt{\pi}} e^{-\frac{x^2}{4a}}, \quad (24)$$

where $a = \Delta E^2$. This technique allows for simultaneous noise reduction, interpolation, calculation of derivatives, and scale

change.¹⁶ The latter is not needed for our data which were measured with equidistant energy steps.

We choose $M = 4$ following the discussions in Refs. 16 and 17, and since we do not see a significant advantage in using M of higher order. Substituting Eq. (24) into Eq. (23)

$$\bar{\epsilon}_4(E) \approx \frac{\pi^{-\frac{1}{2}}\Delta E'}{12\,288\Delta E} \sum_{j=-\infty}^{\infty} \left[\epsilon_j e^{-\frac{(E-E_j)^2}{4\Delta E'^2}} \left(15\,120 - \frac{10\,080(E-E_j)^2}{\Delta E^2} + \frac{1512(E-E_j)^4}{\Delta E^4} - \frac{72(E-E_j)^6}{\Delta E^6} + \frac{(E-E_j)^8}{\Delta E^8} \right) \right], \quad (25)$$

from which we calculate the second derivative

$$\frac{d^2\bar{\epsilon}_4(E)}{dE^2} \approx \frac{\pi^{-\frac{1}{2}}\Delta E'}{49\,152\Delta E^3} \sum_{j=-\infty}^{\infty} \left[\epsilon_j e^{-\frac{(E-E_j)^2}{4\Delta E'^2}} \left(-1\,10880 + \frac{188\,496(E-E_j)^2}{\Delta E^2} - \frac{45\,936(E-E_j)^4}{\Delta E^4} + \frac{3608(E-E_j)^6}{\Delta E^6} - \frac{106(E-E_j)^8}{\Delta E^8} + \frac{(E-E_j)^{10}}{\Delta E^{10}} \right) \right]. \quad (26)$$

Equation (25) can be used to obtain a continuous function of the dielectric function with noise reduction depending on the filter width ΔE , which is chosen according to the white noise onset of the Fourier coefficients obtained from a discrete Fourier transform of the data^{16,17} as illustrated in Fig. 2. The Fourier coefficients C_n of the real (ϵ_1) and imaginary (ϵ_2) part of the dielectric function are obtained from a discrete Fourier transform along with removal of endpoint discontinuities, as described in Ref. 6. Comparing the Fourier transform $B_4(n)$ of the EG filter defined in Eq. (24) (symbols in Fig. 2) with $\ln(C_n)$, it becomes obvious why the right choice of ΔE is crucial to efficiently suppress noise while at the

and approximating the integral as a sum over the data points $f(E_j) = \epsilon_j$, in accordance with Eq. (21c) in Ref. 16 for wavelength-to-energy conversion, we can write the dielectric function for $M = 4$ and equidistant energy steps $\Delta E'$ as

same time preserving information about the line shape contained in the lower order Fourier coefficients.^{16,17} In other words, if ΔE takes on a value that is too small, noise is enhanced and distorts the line shape, while a rather large ΔE broadens the line shape. For most data sets, the filter widths of ϵ_1 and ϵ_2 are chosen to have the same value, but for some cases (such as the one shown in Fig. 2), ϵ_2 requires slightly more filtering. We reach the best compromise between noise reduction and broadening of the line shape due to the filter for a drop of B_4 by approximately 40%–50% at the onset of white noise (similar to Fig. 5 in Ref. 16 and Fig. 2 in Ref. 17). For the data shown in Fig. 2, this corresponds to a filter width of $\Delta E = 0.85$ meV for ϵ_1 and $\Delta E = 0.95$ meV for ϵ_2 , which is about twice the step size ($\Delta E' = 0.4$ meV) and about the same as the instrumental broadening for E_0 at 80 K.

Determining the filter widths from the Fourier coefficients provides a tangible method to set the amount of smoothing for each data set in the same way. For the calculation of the second derivatives of our data, smoothing works slightly better using the EG filter method compared to the commonly used Savitzky-Golay⁹ technique. This is illustrated in Fig. S8 in the supplementary material. In more recent publications, the authors of Ref. 16 point out that the EG filter can be outperformed by either using different filters³⁸ or by exploiting a maximum-entropy method³⁹ to extend the Fourier coefficients beyond the white-noise onset to reconstruct data and generate derivatives that are effectively noise-free. For the purpose of our investigations, we achieve satisfactory results utilizing the EG filters.

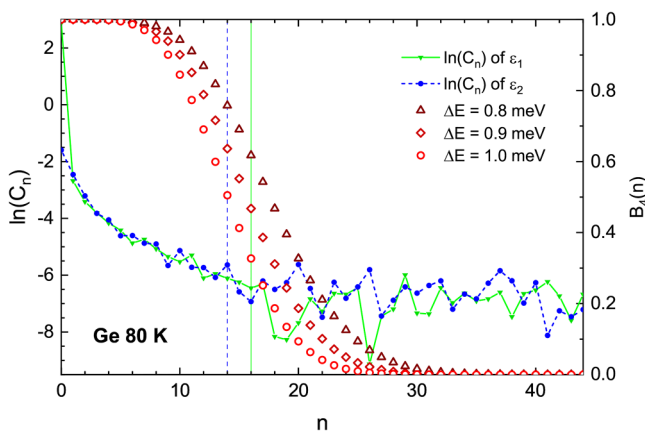


FIG. 2. Natural logarithm of the Fourier coefficient amplitude C_n of the real (ϵ_1) and imaginary (ϵ_2) parts of the dielectric function of Ge at 80 K, obtained as explained in the text. Symbols represent the Fourier transform of the EG filters for $M = 4$ and different ΔE . The vertical lines mark the onset of white noise for ϵ_1 (solid) and ϵ_2 (dashed), respectively. $\Delta E = 0.85$ meV for ϵ_1 and $\Delta E = 0.95$ meV for ϵ_2 are the best choices for this case.

V. FITTING

The fits are performed using a standard Levenberg-Marquardt algorithm,⁴⁰ modified for the possibility of a simultaneous fit of the real and imaginary parts of the dielectric function and their second energy derivatives by calculating a weighted χ^2 . Parts (a) and (b) of Fig. 3 show ϵ_1 and ϵ_2 (dotted lines),

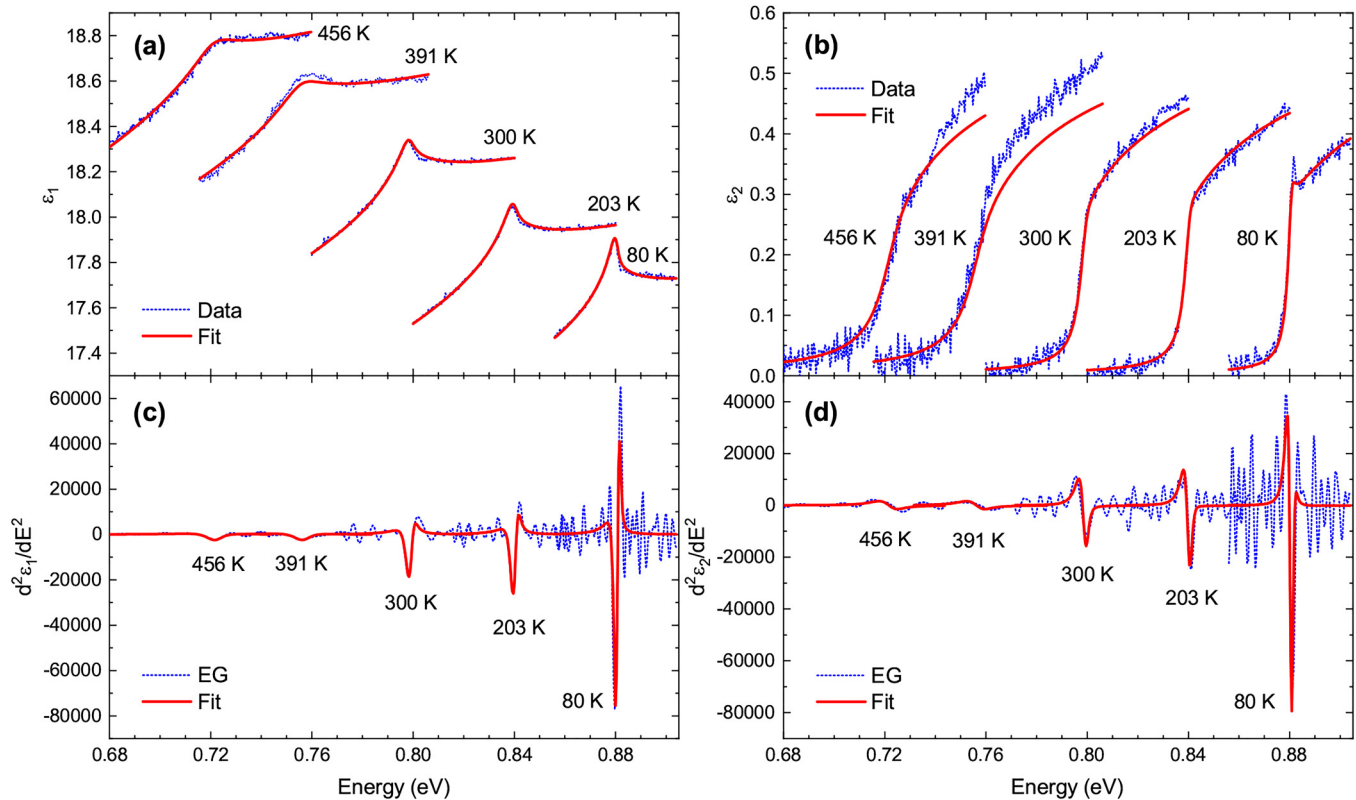


FIG. 3. Real (a) and imaginary (b) parts of the dielectric function and the corresponding second derivatives with respect to energy, (c) and (d), respectively, calculated from Eq. (26) at various temperatures. Solid lines represent the best fits to the data.

respectively, determined through independent fits at each wavelength (point-by-point fits) and corrected for the native oxide layer at various temperatures. Dotted lines in (c) and (d) represent the second derivatives calculated via Eq. (26) and solid lines in (a)–(d) show the fits with Eq. (8). The energy and broadening parameters are fitted to ϵ_1 and ϵ_2 and their second energy derivatives, $d^2\epsilon_1/dE^2$ and $d^2\epsilon_2/dE^2$, while the Sellmeier parameters are fitted to the real part only. Since the hh and lh excitonic peaks cannot be distinguished in our data, we set $\gamma = \gamma_{hh} = \gamma_{lh}$. If the heavy and light hole excitons are split, for example, in a quantum well,⁴¹ in a wurtzite crystal like ZnO or GaN, or under biaxial stress,⁴² it may be possible to determine γ_{hh} and γ_{lh} independently. The agreement between the model and the data right at the bandgap (i.e., in the range of $E_0 \pm 40$ meV) at room temperature and below is remarkable, particularly in view of the fact that amplitudes are not fitted, as in traditional ellipsometry work. At the lowest temperatures (10–110 K), however, while the model provides a good description of the exciton continuum, the excitonic peak, which depends on the broadening, the amount of screening, and the excitonic binding energy, is not described well by the model. The reason for this discrepancy is unclear, but might partly be related to the broadening and to limitations of our additive model for the excitonic contributions of light and heavy holes. Above room temperature, we

observe distortions at about 0.74, 0.77, and 0.8 eV due to xenon lamp spectral line peaks. These distortions seem to affect the second derivatives and the broadening between 370 and 450 K. It may be possible to avoid this problem by taking measurements with a quartz tungsten halogen lamp, which does not have discrete spectral lines. Furthermore, the agreement between the model and the imaginary part ϵ_2 worsens with increasing temperature. This can be explained only to some extent by the uncertainty caused by the native oxide layer correction, see also Sec. S1 in the [supplementary material](#). Changing the oxide layer thickness by 1 Å results in a change in the ϵ_2 magnitude of about 6% (as shown in Fig. S2 in the [supplementary material](#)), while the deviation between model and data at $T > 500$ K is on the order of 10%–25%. This is illustrated in Fig. 4, which shows the fit results of the 690 K measurement. Although it appears that the bandgap energy is off by a few meV and shifting the fit to the left (dashed curve) improves the agreement of the model and ϵ_2 , it worsens the real part and the second derivatives. Hence, we conclude that the problem lies with the amplitude rather than the direct bandgap energy.

We have extended the model to include non-parabolicity and the energy dependence of the momentum matrix element, but we find that the overall effect is negligible for the spectral range of our fits and, therefore, use the simpler formulation for parabolic bands.

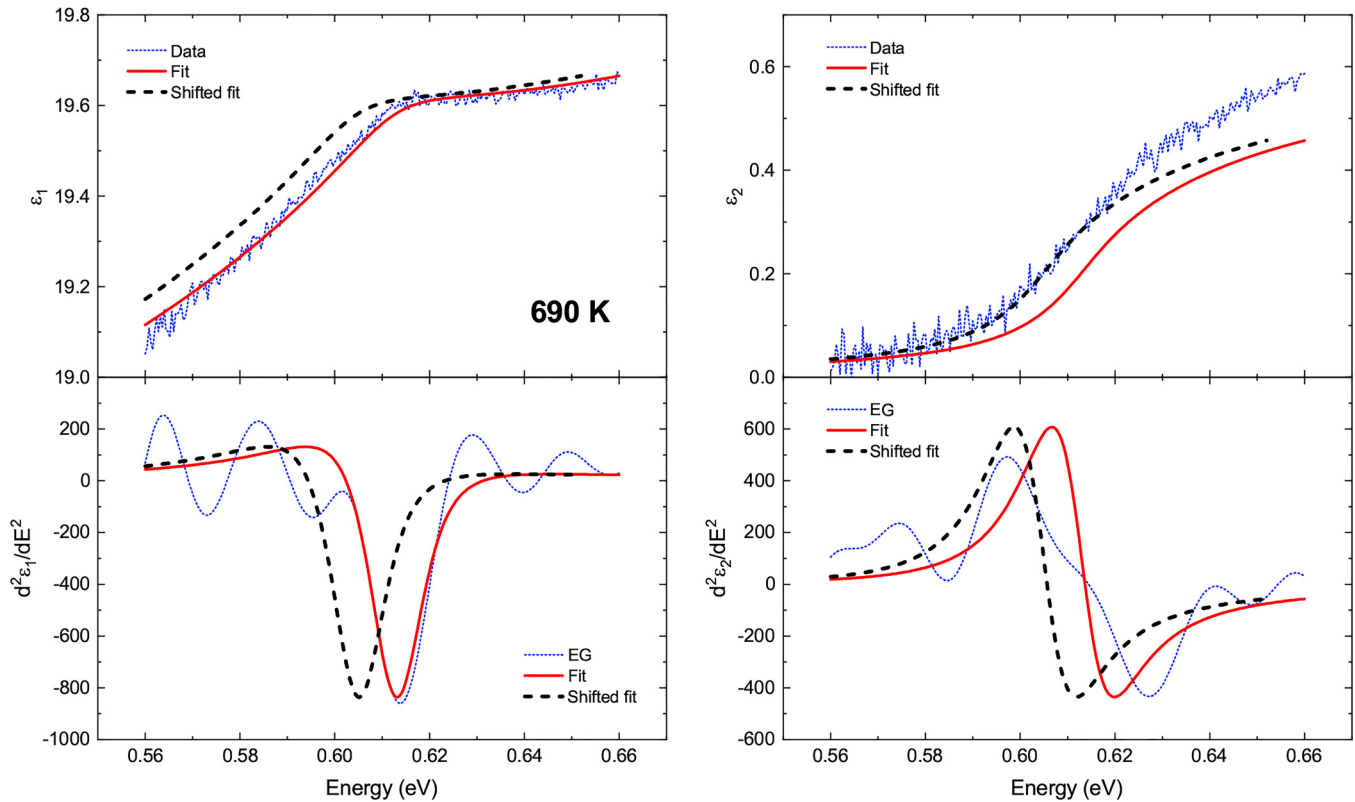


FIG. 4. Like Fig. 3 for a temperature of 690 K, where the solid line represents the best fit to the data and the dashed line shows the fit shifted by 8 meV toward lower energies.

The discrepancies due to non-parabolicity are small for $E - E_0 < 40$ meV and only become important for $E - E_0 > 100$ meV.

Due to the issue with the amplitude, it was necessary for the high-temperature data sets to fit the energies, and in some cases also the broadenings, to the second derivatives only. However, in Fig. S1 in the supplementary material, we plot the model using the fit parameters also for the dielectric function to illustrate that the agreement between model and data is good for ϵ_1 , while this is not the case for ϵ_2 . At the highest temperature (710 K), the energy and broadening were fitted to the second derivative of ϵ_2 only, since $d^2\epsilon_1/dE^2$ is too distorted as a result of noise. Figure S1 in the supplementary material shows the fit results at 598, 639, 676, and 710 K.

VI. TEMPERATURE DEPENDENCE

A. Energy and broadening

Figure 5 shows the temperature dependence of the direct bandgap energy obtained from the fits with Eq. (8) compared to results from Refs. 5 and 35. The temperature dependence of the broadening parameters, which are assumed to be independent of

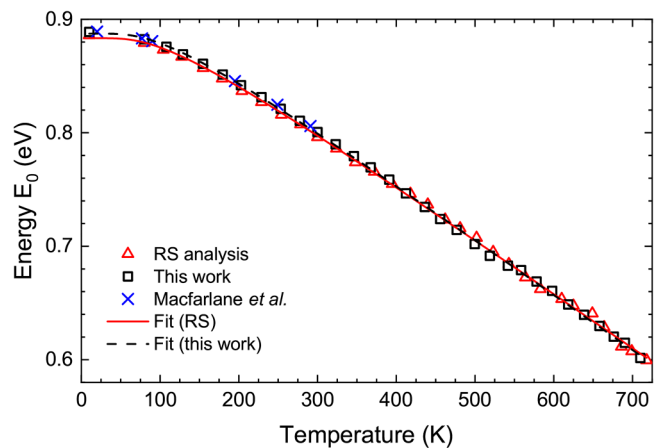


FIG. 5. Temperature dependence of the direct bandgap energy obtained from the fits with Eq. (8) (\square), compared to the results by a reciprocal space analysis⁵ (\triangle) and the results from Macfarlane *et al.*³⁵ (\times). Lines represent fits with Eq. (27).

photon energy, obtained from the Hulthén–Tanguy fits is shown in Fig. 6 along with experimental results by McLean and Paige^{43,44} and Aspnes,⁴⁵ and the broadening calculated according to Eq. (38) in Ref. 21 for $\epsilon = 0$. For the latter, only contributions corresponding to the scattering of electrons with LA and LO phonons are taken into account (for further explanations, see Sec. S2 in the supplementary material). Temperature-dependent phonon energies from Ref. 46 are considered in the calculation, as well as the temperature dependence of the transverse mass using Eqs. (B4) and (B5) in Ref. 20. The deformation potentials (taken from Ref. 21) and the longitudinal mass are assumed to be independent of temperature. For better comparison with the theory, the instrumental resolution is added to the calculated broadening. We note that the agreement between the experimental and predicted broadenings is reasonable up to room temperature. Theory and experiment begin to diverge at the temperatures when the line shape fits begin to worsen. Taking into account the temperature dependence of the screening parameter g reduces the broadening at the highest temperatures by about 10% (see Sec. S2 B in the supplementary material), as shown in Fig. S4, but the agreement with theory and experiment for the dielectric function and its second derivative does not really improve.

To fit the temperature dependence due to electron–phonon interactions, we use the Bose–Einstein model for the energies,⁴⁷

$$E(T) = E_a - E_b \left[1 + 2 / \left(e^{E_{ph}/(k_B T)} - 1 \right) \right], \quad (27)$$

where E_a is the unrenormalized transition energy, E_b is the electron–phonon coupling strength, k_B is the Boltzmann constant, and $E_{ph} = k_B \Theta_{ph}$ is an effective phonon energy. A similar expression

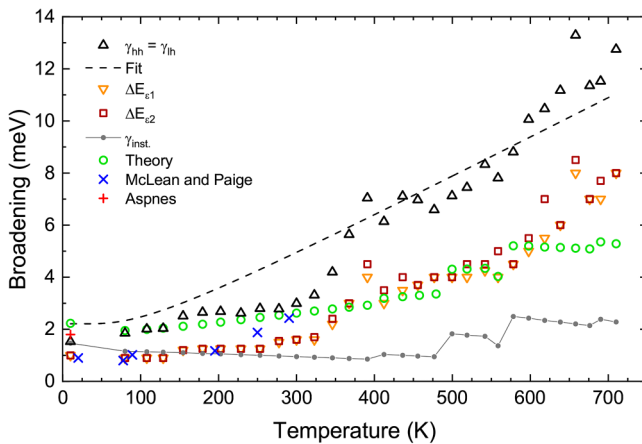


FIG. 6. Temperature dependence of the broadening obtained from the fits with Eq. (8) (Δ), best fit to the data with Eq. (28) (dashed), filter widths used for the real part (∇) and imaginary part (\square), the instrumental resolution (γ_{inst}), calculated width as explained in the text (\circ), and values from McLean and Paige^{43,44} (\times) and Aspnes⁴⁵ ($+$). The hh and lh broadening parameters are forced to have the same value.

TABLE III. Parameters E_a , E_b , and the effective phonon energy E_{ph} obtained from fitting Eq. (27) to the temperature dependent energy E_0 of the direct bandgap for different analysis methods and models.

	E_a (eV)	E_b (eV)	E_{ph} (meV)
This work	0.958 ± 0.002	0.071 ± 0.003	25 ± 1
RS (Ref. 5)	0.953 ± 0.003	0.070 ± 0.004	25 ± 1
SD, 3D (Ref. 5)	0.947 ± 0.004	0.061 ± 0.005	22 ± 2

describes the broadening as a function of temperature,⁴⁷

$$\gamma(T) = \gamma_1 + \gamma_0 \left[1 + 2 / \left(e^{E_{ph}/(k_B T)} - 1 \right) \right]. \quad (28)$$

Equation (28) is an attempt to capture the complex physics of the electron–phonon self-energies in a simple expression that uses an effective phonon frequency. It is helpful as a compact parametrization of the experimental data. The fits with the above equations are shown by the various lines in Figs. 5 and 6, and the fit parameters in Eqs. (27) and (28) are listed in Tables III and IV. We find $E_0 = 888.8 \pm 0.6$ meV at 10 K and $E_0 = 882.4 \pm 0.7$ meV at 80 K, which compare well to the energies reported by Nishino *et al.*⁴⁹ (889.0 meV at 24 K and 881.4 meV at 83 K) and Macfarlane *et al.*³⁵ (889.2 meV at 20 K and 883.2 eV at 77 K). Aspnes⁴⁵ found $E_0 = 887.2$ meV and the excitonic energy $E_{ex} = 885.8 \pm 0.5$ meV, as well as a broadening of 1.8 ± 0.3 meV at 10 K.

B. Effective masses and excitonic binding energies

The decrease in the effective masses between 10 and 710 K is 29% for $m_{e\Gamma}$ and m_{lh} and 9% for m_{hh} according to Eqs. (11)–(13). The major contribution to the temperature dependence of the effective masses stems from the energies E_0 (Fig. 5) and E'_0 via the DKK parameters defined in Eqs. (14)–(16) since the changes due to thermal expansion of the matrix elements are small. This temperature dependence of the effective masses also leads to a temperature-dependent excitonic binding energy. According to Ref. 50, the excitonic binding energy is proportional to the direct bandgap energy, $R_h \propto E_0$, illustrated by the dotted line in Fig. 7. Our results do not satisfy this relation. Instead, we find

$$R_{hh}(E_0) = 2.158(5)E_0^{1.549(8)}$$

TABLE IV. Parameters obtained by fitting Eq. (28) to the temperature dependent broadening, where $\gamma_1 = 0$ and the effective phonon energy was fixed to the value obtained from fitting the energy (see Table III). Calculated values from Ref. 48 are listed for comparison.

	γ_0 (meV)	E_{ph} (meV)
This work	2.21 ± 0.06	25 (fixed)
Theory (Ref. 48)	1.459 ± 0.001	27.6 ± 0.2

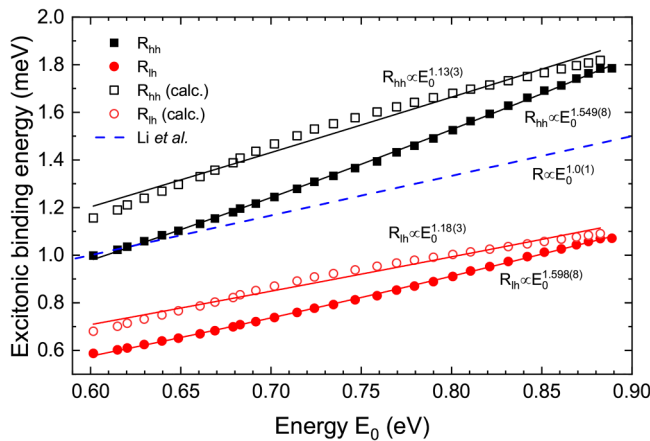


FIG. 7. Excitonic binding energies of the heavy-hole (R_{hh}) and light-hole (R_{lh}) excitons calculated from Eq. (10) vs energy E_0 of the direct bandgap (which varies with temperature, as shown in Fig. 5). Closed symbols depict R_{hh} and R_{lh} calculated using ϵ_{st} from extrapolating ϵ_1 to lower energies (symbols in Fig. 8) and open symbols show R_{hh} and R_{lh} calculated using Eq. (29) (line in Fig. 8). Solid lines represent fits with $R(E_0) = bE_0^X$ and the dashed line represents the extension to lower energies of the curve shown in Fig. 5 of Ref. 50 with $R_l \propto E_0^{1.0(1)}$.

and

$$R_{lh}(E_0) = 1.302(3)E_0^{1.598(8)}.$$

Only two parameters affect the excitonic binding energy: the reduced mass and the static dielectric constant ϵ_{st} . We obtain ϵ_{st} , which is equal to the high-frequency dielectric constant ϵ_∞ in the case of Ge, from our data by extrapolating the fit of the dielectric

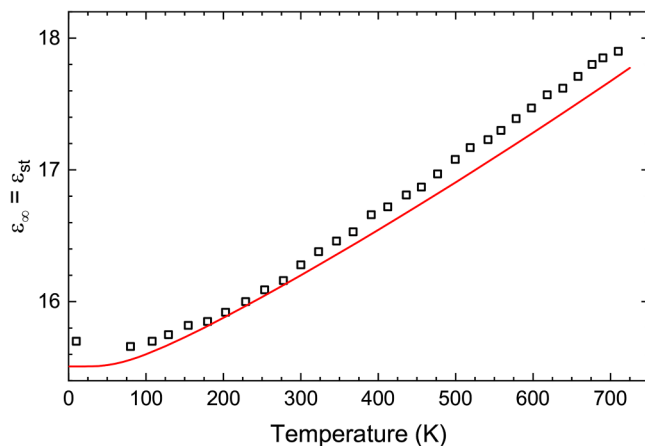


FIG. 8. Temperature dependence of the high-frequency dielectric constant ϵ_∞ of Ge obtained from the experimental data (symbols) compared with ϵ_∞ calculated from Eq. (29) (line) using the literature value⁵² $\epsilon_\infty(T = 300 \text{ K}) = 16.2$.

function with a parametric oscillator model¹⁰ to very low energies. Figure 8 shows how ϵ_∞ increases with temperature, mostly due to the decrease in the Penn gap E_{Penn} via¹

$$\epsilon_\infty(T) = 1 + \left(\frac{E_u}{E_{\text{Penn}}(T)} \right)^2. \quad (29)$$

We use $E_u = \hbar\omega_u = 15.6 \text{ eV}$ for Ge, which is calculated from the plasma frequency ω_u , and assume that E_{Penn} and E_2 (the critical point at about 4.5 eV, see Ref. 1) have the same temperature dependence.⁵¹ Taking the latter from Ref. 25 and $\epsilon_\infty = 16.2$ at room temperature from the literature,⁵² we can write the temperature dependence of the Penn gap as

$$E_{\text{Penn}}(T) = (4.146 \text{ eV}) - (0.05 \text{ eV}) \left(\frac{2}{e^{\frac{217\text{K}}{T}} - 1} + 1 \right). \quad (30)$$

We find a reasonable agreement between the high-frequency dielectric constant calculated from Eq. (29) (line in Fig. 8) and the values we obtain from the extrapolation of our data (symbols in Fig. 8) up to room temperature. Using Eq. (29) to calculate R_{hh} and R_{lh} results in

$$R_{hh}(E_0) = 2.14(2)E_0^{1.13(3)}$$

and

$$R_{lh}(E_0) = 1.29(1)E_0^{1.18(3)}.$$

The effective masses used to compute R_{hh} and R_{lh} depend on the fit parameter E_0 as outlined in Sec. III.

VII. CONCLUSIONS

Several assumptions and simplifications were made to the theory. First, we simply added two Hulthén–Tanguy terms, one for the hh and one for the lh, instead of solving a complicated three-body problem. Second, the contribution of the split-off band was ignored since it only affects the real part of the dielectric function and the small effect can be compensated by adjusting the Sellmeier parameters. Third, we did not consider warping and non-parabolicity. The latter results in a deviation between the model and the data starting at about 100 meV above the bandgap. Furthermore, we ignore the indirect bandgap, which affects E_0 due to the resonant character of the direct and indirect bandgaps.²⁰ An experimental and theoretical study thereof is given in Ref. 20. This effect might be important for Ge because the indirect bandgap lies only about 0.15 eV below the direct gap.^{32,53} Finally, we only fit the bandgap energy and broadening, but no adjustable parameter that would affect the magnitude of the imaginary part. In principle, this theory can also be applied to other semiconductors with similar band structures such as GaAs, InSb, or germanium–tin alloys.

In summary, we fitted the Hulthén–Tanguy model to the dielectric function and its second derivatives and find the model to be in good agreement with our data up to room temperature. Discrepancies at higher temperatures might be partly due to the above-mentioned simplifications of the theory and partly due to

the challenging experimental conditions at high temperatures. Improvements to the model and investigations of electron–phonon scattering processes will be addressed in future work.

SUPPLEMENTARY MATERIAL

See the [supplementary material](#) for discussion on the broadening of the direct bandgap and the limitations due to instrumental resolution, noise, and the digital linear filter. Furthermore, a brief discussion of the second derivatives obtained from the EG filter method and Savitzky–Golay coefficients and fit results at some selected high temperatures are provided.

ACKNOWLEDGMENTS

This work was supported by Air Force Office of Scientific Research under Award No. FA9550-20-1-0135, the National Science Foundation (NSF, Nos. DMR-1505172 and DMR-2119583), and from Operational Programme Research, Development and Education—Project “Postdoc2MUNI” (No. CZ.02.2.69/0.0/0.0/18_053/0016952).

AUTHOR DECLARATIONS

Conflict of Interest

The authors have no conflicts to disclose.

DATA AVAILABILITY

The data that support the findings of this study are available from the corresponding author upon reasonable request.

REFERENCES

- ¹P. Y. Yu and M. Cardona, *Fundamentals of Semiconductors: Physics and Materials Properties* (Springer-Verlag, Berlin, 1996).
- ²R. J. Elliott, *Phys. Rev.* **108**, 1384 (1957).
- ³C. Tanguy, *Phys. Rev. Lett.* **75**, 4090 (1995).
- ⁴C. Tanguy, *Phys. Rev. B* **60**, 10660 (1999).
- ⁵C. Emminger, F. Abadizaman, N. S. Samarasingha, T. E. Tiwald, and S. Zollner, *J. Vac. Sci. Technol., B* **38**, 012202 (2020).
- ⁶S. D. Yoo and D. E. Aspnes, *J. Appl. Phys.* **89**, 8183 (2001).
- ⁷M. Cardona, *Modulation Spectroscopy*, edited by F. Seitz, D. Turnbull, and H. Ehrenreich (Academic, New York, 1969).
- ⁸D. E. Aspnes, *Handbook on Semiconductors*, edited by M. Balkanski (North-Holland, Amsterdam, 1980).
- ⁹A. Savitzky and M. J. E. Golay, *Anal. Chem.* **36**, 1627 (1964).
- ¹⁰C. M. Herzinger and B. Johs, U.S. patent 5,796,983 (18 August 1998).
- ¹¹V. R. D’Costa, Y. Fang, J. Mathews, R. Roucka, J. Tolle, J. Menéndez, and J. Kouvetakis, *Semicond. Sci. Technol.* **24**, 115006 (2009).
- ¹²R. Roucka, R. Beeler, J. Mathews, M.Y. Ryu, Y. Kee Yeo, J. Menéndez, and J. Kouvetakis, *J. Appl. Phys.* **109**, 103115 (2011).
- ¹³L. Hulthén, *Ark. Mat. Astron. Fys.* **28A**, 1 (1942).
- ¹⁴A. Ferreira da Silva, *Phys. Rev. B* **37**, 4799 (1988).
- ¹⁵D. E. Aspnes, V. L. Le, and Y. D. Kim, *J. Vac. Sci. Technol., B* **37**, 051205 (2019).
- ¹⁶V. L. Le, T. J. Kim, Y. D. Kim, and D. E. Aspnes, *J. Vac. Sci. Technol., B* **37**, 052903 (2019).
- ¹⁷V. L. Le, T. J. Kim, Y. D. Kim, and D. E. Aspnes, *J. Korean Sci. Phys. Soc.* **77**, 819 (2020).
- ¹⁸D. K. Hoffman, T. L. Marchioro, M. Arnold, Y. Huang, W. Zhu, and D. J. Kouri, *J. Math. Chem.* **20**, 117 (1996).
- ¹⁹D. K. Hoffman, D. J. Kouri, and E. Pollak, *Comput. Phys. Commun.* **147**, 759 (2002).
- ²⁰J. Menéndez, D. J. Lockwood, J. C. Zwickels, and M. Noël, *Phys. Rev. B* **98**, 165207 (2018).
- ²¹J. Menéndez, C. D. Poweleit, and S. E. Tilton, *Phys. Rev. B* **101**, 195204 (2020).
- ²²J.A. Woollam Co., Inc., Lincoln, Model V-VASE.
- ²³D. B. Cuttris, *Bell Syst. Tech. J.* **40**, 509 (1961).
- ²⁴T. N. Nunley, N. S. Fernando, N. Samarasingha, J. M. Moya, C. M. Nelson, A. A. Medina, and S. Zollner, *J. Vac. Sci. Technol., B* **34**, 061205 (2016).
- ²⁵N. S. Fernando, T. N. Nunley, A. Ghosh, C. M. Nelson, J. A. Cooke, A. A. Medina, S. Zollner, C. Xu, J. Menendez, and J. Kouvetakis, *Appl. Surf. Sci.* **421**, 905 (2017).
- ²⁶J. Šik, J. Hora, and J. Humlíček, *J. Appl. Phys.* **84**, 6291 (1998).
- ²⁷F. A. Jenkins and H. E. White, *Fundamentals of Optics*, 4th ed. (McGraw-Hill, New York, 1957), p. 482.
- ²⁸B. Tattian, *Appl. Opt.* **23**, 4477 (1984).
- ²⁹E. O. Kane, *J. Phys. Chem. Solids* **1**, 82 (1956).
- ³⁰E. O. Kane, *J. Phys. Chem. Solids* **1**, 249 (1957).
- ³¹M. Cardona, *J. Phys. Chem. Solids* **24**, 1543 (1963).
- ³²M. Hobden, *J. Phys. Chem. Solids* **23**, 821 (1962).
- ³³C. Persson and U. Lindefelt, *J. Appl. Phys.* **82**, 5496 (1997).
- ³⁴G. Dresselhaus, A. Kip, and C. Kittel, *Phys. Rev.* **98**, 368 (1955).
- ³⁵G. G. Macfarlane, T. P. McLean, J. E. Quarrington, and V. Roberts, *Proc. Phys. Soc.* **71**, 863 (1958).
- ³⁶P. Lawaetz, *Phys. Rev. B* **4**, 3460 (1971).
- ³⁷L. M. Roth, B. Lax, and S. Zwerdling, *Phys. Rev.* **114**, 90 (1959).
- ³⁸V. L. Le, Y. D. Kim, and D. E. Aspnes, *Opt. Express* **28**, 38917 (2020).
- ³⁹V. L. Le, T. J. Kim, Y. D. Kim, and D. E. Aspnes, *J. Appl. Phys.* **129**, 224902 (2021).
- ⁴⁰S. A. Teukolsky, B. P. Flannery, W. H. Press, and W. T. Vetterling, *Numerical Recipes in C* (Press Syndicate of the University of Cambridge, New York, 1992), Chap. 15.5.
- ⁴¹J. Humlíček, E. Schmidt, L. Bočánek, R. Švehla, and K. Ploog, *Phys. Rev. B* **48**, 5241 (1993).
- ⁴²S. Logothetidis, M. Cardona, and C. Trallero-Giner, *J. Appl. Phys.* **67**, 4133 (1990).
- ⁴³T. P. McLean and E. G. S. Paige, *J. Phys. Chem. Solids* **23**, 822 (1962).
- ⁴⁴T. P. McLean and E. G. S. Paige, in *Proceedings of the International Conference on the Physics of Semiconductors*, edited by A. C. Stickland (Institute of Physics, London, 1962), Vol. 450.
- ⁴⁵D. E. Aspnes, *Phys. Rev. B* **12**, 2297 (1975).
- ⁴⁶G. Nelín and G. Nilsson, *Phys. Rev. B* **10**, 612 (1974).
- ⁴⁷L. Viña, S. Logothetidis, and M. Cardona, *Phys. Rev. B* **30**, 1979 (1984).
- ⁴⁸P. Lautenschlager, P. B. Allen, and M. Cardona, *Phys. Rev. B* **33**, 5501 (1986).
- ⁴⁹T. Nishino, T. Yanagida, and Y. Hamakawa, *J. Phys. Soc. Jpn.* **30**, 579 (1971).
- ⁵⁰G. H. Li, A. R. Goñi, K. Syassen, and M. Cardona, *Phys. Rev. B* **49**, 8017 (1994).
- ⁵¹N. S. Samarasingha and S. Zollner, *J. Vac. Sci. Technol., B* **39**, 052201 (2021).
- ⁵²F. A. D’Altroy and H. Y. Fan, *Phys. Rev.* **103**, 1671 (1956).
- ⁵³G. G. Macfarlane, T. P. McLean, J. E. Quarrington, and V. Roberts, *J. Phys. Chem. Solids* **8**, 388 (1959).